Ligand-Induced Surface Charge Density Modulation Generates Local Type-II Band Alignment in Reduced-Dimensional Perovskites

Rafael Quintero-Bermudez,†,∇ Andrew H. Proppe,†,‡,∇ Arup Mahata,§,∥,∇ Petar Todorović´, † Shana O. Kelley,‡,⊥ Filippo De Angelis,*,§,∥,# and Edward H. Sargent*,†

† Department of Electrical and Computer Engineering, University of Toronto, 10 King's College Road, Toronto, Ontario M5S 3G4, Canada

‡ Department of Chemistry, University of Toronto, 80 St George Street, Toronto, Ontario M5S 3G4, Canada
§ D3-Computation, Istituto Italiano di Tecnologia, 16163 Genova, Italy

∥ Computational Laboratory for Hybrid/Organic Photovoltaics (CLHYO), Istituto CNR di Scienze e Tecnologie Molecolari (ISTM-CNR), Via Elce di Sotto 8, 06123 Perugia, Italy

⊥Department of Pharmaceutical Sciences, Leslie Dan Faculty of Pharmacy, University of Toronto, Toronto, Ontario M5S 3M2, Canada

Department of Chemistry, Biology and Biotechnology, University of Perugia, Via Elce di Sotto 8, 06123 Perugia, Italy

ABSTRACT: Two-dimensional (2D) and quasi-2D perovskite materials have enabled advances in device performance and stability relevant to a number of optoelectronic applications. However, the alignment among the bands of these variably quantum confined materials remains a controversial topic: there exist multiple experimental reports supporting type-I, and also others supporting type-II, band alignment among the reduced-dimensional grains. Here we report a combined computational and experimental study showing that variable ligand concentration on grain surfaces modulates the surface charge density among neighboring quantum wells. Density functional theory calculations and ultraviolet photoelectron spectroscopy reveal that the effective work function of a given quantum well can be varied by modulating the density of ligands at the interface. These induce type-II interfaces in otherwise type-I aligned materials. By treating 2D perovskite films, we find that the effective work function can indeed be shifted down by up to 1 eV. We corroborate the model via a suite of pump−probe transient absorption experiments: these manifest charge transfer consistent with a modulation in band alignment of at least 200 meV among neighboring grains. The findings shed light on perovskite 2D band alignment and explain contrasting behavior of quasi-2D materials in light-emitting diodes (LEDs) and photovoltaics (PV) in the literature, where materials can exhibit either type-I or type-II interfaces depending on the ligand concentration at neighboring surfaces.
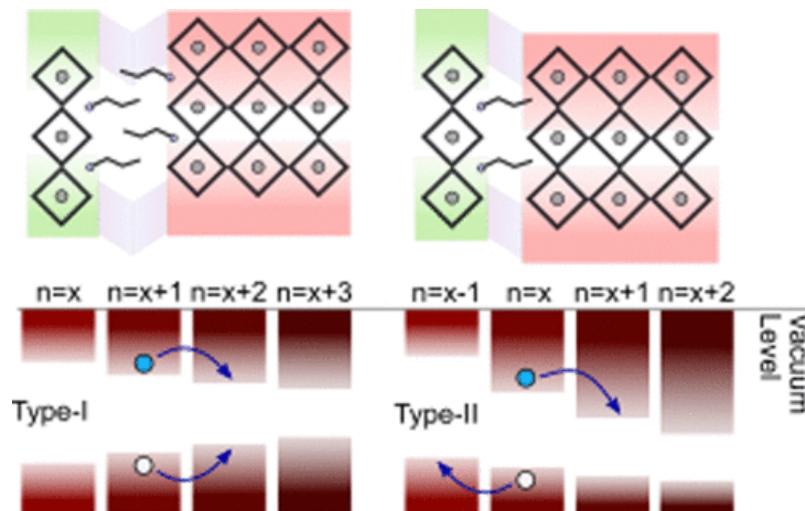
INTRODUCTION

The metal-halide perovskite material system has enabled remarkable advances in photovoltaics(1−4) and light-emitting devices.(5−9) Its cubic ABX_3 crystal structure offers wide tunability of the bandgap via elemental composition. In addition, this class of materials exhibits high charge carrier mobilities,(10) high tolerance to and low density of electronic trap states,(11,12) low energetic barriers to materials formation,(13) and an anticipated low cost of fabrication.

Reduced-dimensional (2D and quasi-2D) metal-halide perovskites (RDPs),(14,15) such as Ruddlesden–Popper or Dion–Jacobson phase perovskites, are synthesized with large intercalating cations (such as phenethylammonium (PEA) and *n*-butylammonium (BTA)). These have garnered attention due to their increased long-term stability and high photoluminescence quantum yield (PLQY), which have enabled long operational stability in devices(16−18) and bright high-efficiency LEDs,(19,20) respectively. The crystal system exhibits the $R_2A_{n-1}B_nX_{3n+1}$ structure where R is the intercalating cation and *n* represents the number of perovskite layers in a well. This notation can be used to represent 3D ($n \rightarrow \infty$), 2D ($n = 1$), and quasi-2D ($n > 1$) (Figure 1a).
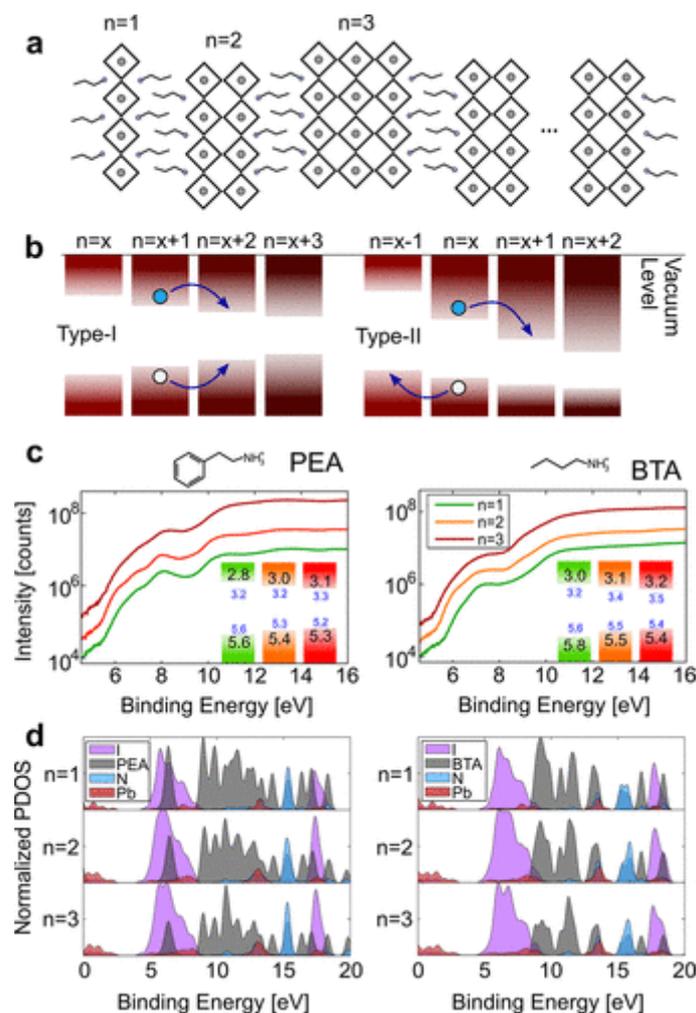

Figure 1. Band alignment of BTA and PEA RDP single crystals. (a) Graphical depiction of RDPs. (b) Schematic of type-I and type-II RDP alignment and transfer enabled in each case. (c) UPS of *n* = 1, 2, and 3 RDPs, valence and conduction band edges determined

experimentally (black) and computationally (blue) (inset). UPS measurements reveal type-I alignment among RDPs. (d) Calculated projected density of states (PDOS) for $n = 1, 2$, and 3 RDPs by HSE-SOC.

The energies of the valence and conduction band edge levels in semiconductors are central to optoelectronic device design. The ionization energy (IE), electron affinity (EA), and work function (Wf) inform the selection of transport layers and contacts to minimize turn-on voltage, ensure charge balance in LEDs, maximize V_{oc}, and minimize parasitic resistances in PV. The band alignment of RDPs remains a controversial topic, given apparent contradictions in experimental data in the literature. Whereas some studies have found that RDPs exhibit an unconventional type-II band alignment as the number of layers n is increased,[7,19,21] others report a typical type-I band alignment between these different phases.[22]

Here, we report the positioning of conduction and valence band edges of PEA- and BTA-based RDPs of $n = 1, 2$, and 3, all the while mitigating sources of misinterpretation. With the aid of density functional theory (DFT) and ultraviolet photoelectron spectroscopy (UPS), we report that the effective Wf of a given quantum well can be varied by the density of ligands at the interface. By surface-treating 2D perovskite films, we find that the effective Wf can be reduced by up to 1 eV. This can induce type-II interfaces among neighboring RDP phases. The model is then corroborated by a series of pump–probe transient absorption (TA) experiments that evidence selective transfer resulting from these band misalignments in an untreated film.

This work has direct consequences on our understanding of 2D, quasi-2D, and mixed 2D/3D devices because these misalignments can form unintentionally in solution-processed RDP films but can also be systematically engineered. The results of these studies rationalize how mixed-dimensional films of well- and homogeneously passivated quantum wells have a type-I alignment, forming an energy cascade that drives efficient exciton transfer without charge separation. At the same time, 2D/3D heterostructures used in efficient photovoltaics can now be understood as exhibiting type-II interfaces, whereby upshifted 2D quantum wells may block charge transport for electrons but retain efficient hole transport due to alignment of the 2D and 3D valence bands.

Results

Single-Crystal Band Levels

Confinement modeled by an infinite potential well in quantum mechanics finds that the valence and conduction band edges are raised and lowered, respectively, by a magnitude that is a function of the width of the confinement and the effective mass of the charge carrier.[23] Therefore, under this framework a type-I band alignment is expected to result as quantum confinement increases the bandgap of RDPs (Figure 1b). Numerous reports in the literature, however, report that RDP films form type-II or quasi-type-II alignments as the number of layers, n, is increased.[7,19,21] In support of this alignment, ultrafast TA studies have shown that charge carriers indeed transfer from high-n to low-n RDPs in a film.[4,24]

On the other hand, RDPs have been found to exhibit high PLQYs for the lowest bandgap phases in a film despite a broad distribution of quantum well (QW) thicknesses, evidencing funneling of both electrons and holes toward high-n RDPs.[19,25,26] Funneling from low-to-high n QWs over a wide range of time scales (fs–ns) has also been observed by TA.[19,27] This finding would instead support type-I alignment between RDPs of increasing n. Furthermore, in alignment with this framework, Silver et al. recently investigated the IE and EA of BTA $n = 1$ films by a mix of experimental and computational studies with the conclusion that $n = 1$ exhibits type-I alignment with MAPbX$_3$ bulk perovskite.[22]

These conflicting reports of type-I and type-II band alignments among RDPs have propagated in citing literature, leading to contradictory explanations for optoelectronic device performance across the perovskite research community, some attributing their performance to type-I alignments,[19,28,29] some attributing it to type-II alignments,[30−32] and some speculating that their devices are pure phase making RDP interfaces irrelevant.[3] One source of inconsistency in RDP band alignment studies could be attributed to film inhomogeneity. It has been found that RDP films exhibit a wide distribution of well thicknesses.[27] This makes the interpretation of ionization energy measurements of RDP films difficult. Furthermore, the bandgap distribution in RDP films can even vary across the film thickness,[27] such that the surface distribution might not reflect the average across the entire film n. This property could affect surface-sensitive measurements such as UPS, where the probing depth is typically 20–30 Å depending on the material.[33]

A common technique for determining the valence band edge in semiconductors involves a linear extrapolation to zero to determine the photoemission onset in UPS. Previous studies have noted that this analysis, although successful in epitaxial semiconductors, can be difficult to perform and easily misinterpreted in solution-processed materials due to the low density of states (DOS) near the band edge in such materials.[34,35] Determining the onset, therefore, is more dependable with photoemission data in a logarithmic scale. Processing UPS data for solution-processed materials in a logarithmic scale, however, is not yet standard practice, which could embody further sources of disagreement.

To determine valence and conduction band edges in RDPs while mitigating sources of misinterpretation, we therefore analyze BTA and PEA perovskite single crystals of $n = 1$, 2, and 3 (Figure S10). These measurements are performed on crystals aligned with the (001) axis normal to the substrate (i.e., RDPs parallel to substrate), to reduce surface-dependent variations in photoemission onset.[36,37] Valence spectra for these crystals are shown in Figure 1c. The valence band edge is determined by linearly fitting the photoemission onset in a logarithmic scale. Conduction band edges are determined by subtracting the bandgap from the valence band edge. The bandgap of each RDP phase is computed by adding the exciton binding energy[38,39] to the exciton resonance energy observed in absorption spectra (Figure S9).

The projected density of states (PDOS) were simulated by carrying out hybrid DFT calculations (with HSE) including spin–orbit coupling (SOC) in order to identify features in the RDP valence spectra (Figure 1d). The valence spectra for all RDP samples exhibit clear

features that can be attributed primarily to I 5p orbitals at the band edge, and ligand orbitals at higher binding energies, in agreement with previous computational work.[(22,40)] From these calculations, we see that the predicted valence and conduction band edge energies match well with our experimentally determined values, consistent with a type-I alignment from low-to-high n RDPs.

Taken together, this series of experimental measurements and calculations find that both PEA- and BTA-based RDPs exhibit type-I alignment. This is in agreement with the studies of Silver et al. on $n = 1$ BTA films, which are the only value of n for RDP films that will yield a pure phase due to the lack of A$^+$ cations in the synthesis. The results however, do disagree with the literature supporting a type-II alignment among RDPs.

Surface Charge Density Modulation in Ammonium-Terminated Ligands

Surface charge density modulations (SCDMs) have been known to shift the effective Wf of materials. There are two main phenomena behind this behavior: (1) oriented dipole moments between surface interfaces and (2) surface charge redistribution due to species adsorption. Wf shifts due to oriented dipole moments have been observed in a variety of systems and interfaces, including semiconductor–semiconductor[(41,42)] and semiconductor–metal.[(43−45)] We posited that, in RDPs, oriented dipole moments across ligands could enact such Wf shifts that could, in turn, misalign energy levels with respect to neighboring RDPs ([Figure 2]a). Likewise, the adsorption of such ligands at RDP surfaces could induce charge redistribution at the interface, resulting in similar band edge shifts, as has been observed in TiO$_2$/dye interfaces.[(46)] As was observed in the latter system, it is likely that both oriented dipole moments and surface charge redistribution would take place in RDPs.
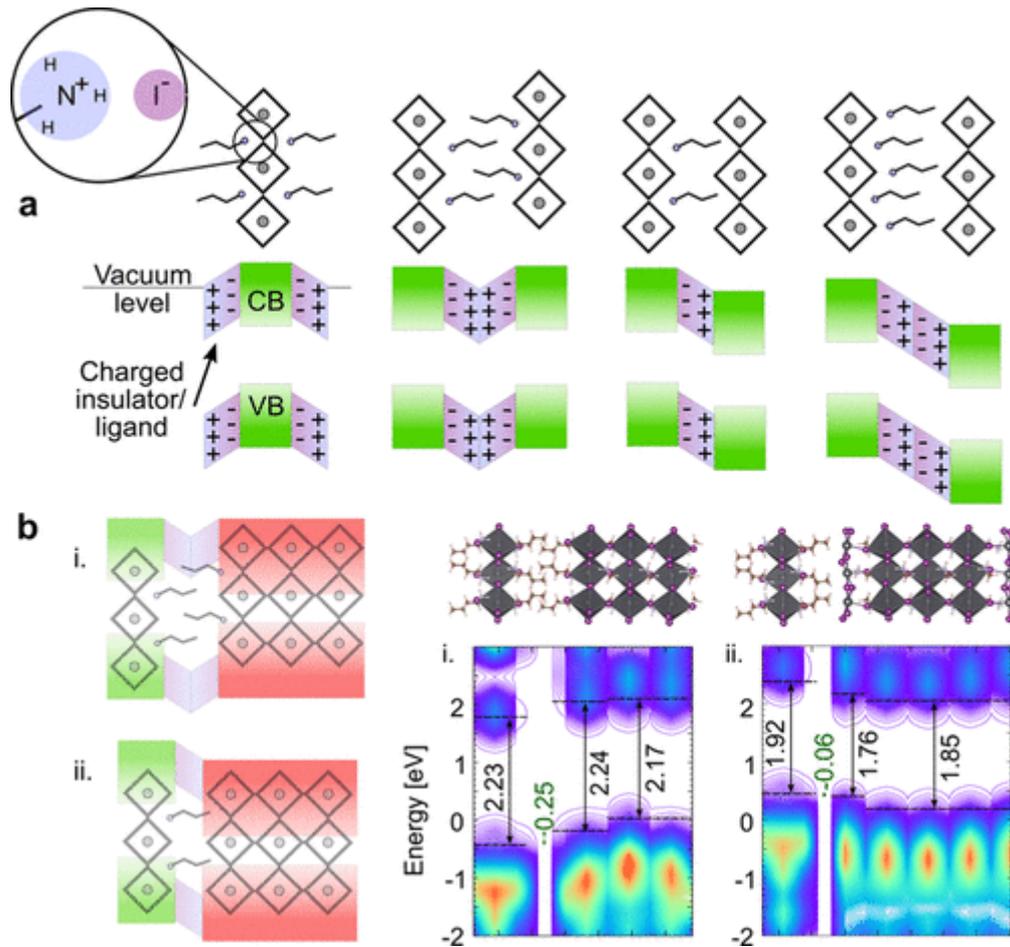
Figure 2. SCDMs enacted by ligands induce type-II RDP interfaces. (a) Schematics depict how dipole moments in RDP ligands could reduce the effective Wf and misalign the energy levels of neighboring RDPs. (b) DFT calculations show that varying the concentration of ligands at the RDP interface can induce type-II interfaces. Because of neglect of SOC, only the alignment of the valence band is accurate, revealing the formation of type-I and type-II interfaces resulting from contrasting ligand concentrations at the interface.

Under this framework, a fully passivated RDP would exhibit a lower Wf than an unpassivated one, and increasing the concentration of ligands on one surface would effectively raise its bands with respect to a neighboring RDP (Figure 2a).

These Wf shifts become particularly interesting at the interface of two RDPs of different n with contrasting ligand concentrations at the interface. We used DFT calculations to determine the band alignment at a mixed RDP interface with and without ligands on one surface (Figure 2b). We modeled an $n = 1/n = 3$ interface in two contrasting scenarios: (i) the $n = 3$ phase is passivated by a layer of PEAI ligands, and (ii) the $n = 3$ layer is completely depleted of PEAI. Because of the large size of these simulations, we report here only Perdew–Burke–Ernzerhof (PBE) results without SOC. In this case, we expect a reasonably accurate alignment only for the valence band. We find that, whereas the former exhibits the expected type-I interface, the $n = 1$ bands in the latter are upshifted to the point of inducing a type-II interface. Interestingly, these structures exhibit significant differences (0.25 vs −0.06 eV) in valence band edge offsets at the $n = 1/n = 3$ interface. This suggests that, with sufficiently

contrasting ligand concentrations on the RDP surfaces at the interface, the Wf shifts illustrated in Figure 2a could lead to a type-II interface.

To investigate relative contributions to the SCDMs imparted by dipole moments versus by charge redistribution, we computed the charge transfer in structures i and ii in Figure 2b. In this scenario, there is a band offset of 0.3 eV in going from a BAI-terminated to a PbI_2-terminated $n = 3$ that is interfaced with a BAI-terminated $n = 1$. The charge transfer calculations indicate that 0.02 and 0.1 eV are transferred for the BAI-terminated (Figure S6a) and the PbI_2-terminated (Figure S6b) structures, respectively. This suggests that the dipole moment contribution in this case could account for the remaining 0.2 eV. Further calculations ensured that both dipole moments and charge redistribution maintain contributions of similar magnitude when the ligand density is varied (Figure S7). We conclude that both dipole moment and surface charge redistribution produced by these ligands will lead to bandshift contributions of a similar magnitude.

We next sought to quantify the magnitude of Wf shifts effected by ligands in RDP surfaces. To do so, we explored surface treatments that could alter the surface distribution of exposed PEAI/PbI_2 on RDP films without degrading or modifying the material. Isopropanol (IPA) treatment solutions containing variable concentrations of PEAI ligands were found to be suitable at treating surfaces without degrading the underlying film. The $n = 1$ films were investigated for this study due to their purity in phase and versatility over single crystals for spin-casting. Given the absence of A^+ cation in the formation of $n = 1$ films, it is not possible to form QWs of $n > 1$ with these treatments. The QW distribution, therefore, cannot be altered.

X-ray photoelectron spectroscopy (XPS) was measured on PEAI-treated and PbI_2-treated $n = 1$ films to ascertain the elemental composition and relative stoichiometry of the exposed surface after the various treatments (Figure S12). The atomic ratios determined from integrating Pb, I, N, and C XPS spectra confirm that soaking the $n = 1$ films with PEAI treatment solutions of increasing concentration results in a greater concentration of PEAI on the film's surface, evidenced by the higher counts from C and N occurring simultaneously with lower counts for Pb (Figure 3a). Similarly, PbI_2 treatments lead to reduced N and C content but an increase in Pb content.
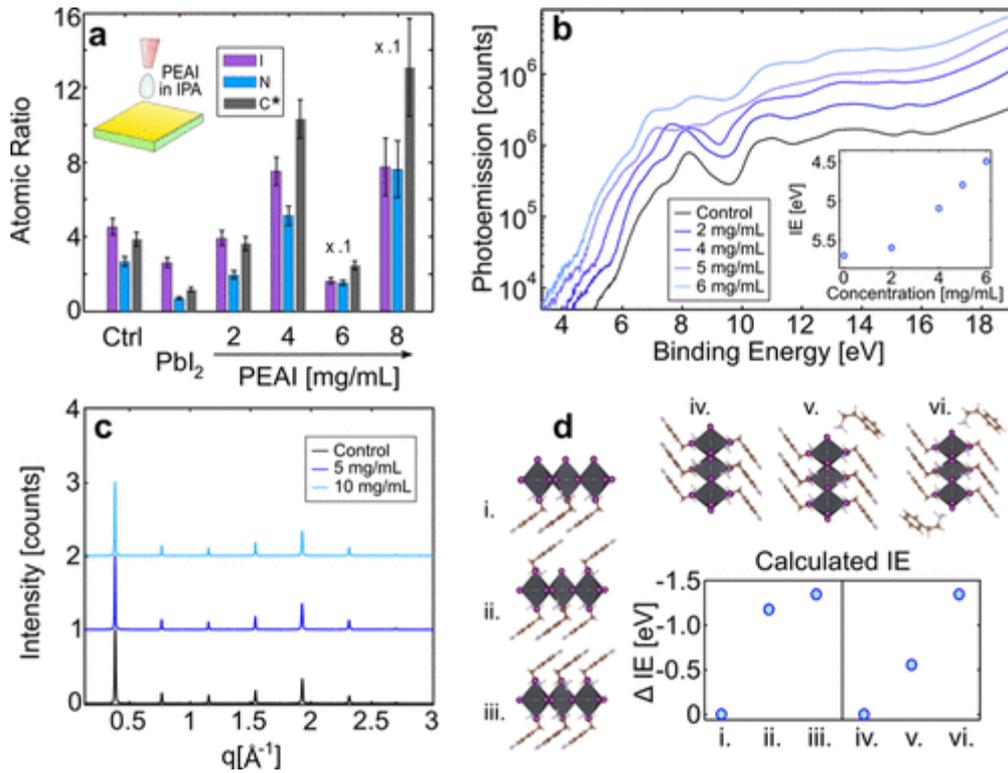
Figure 3. Film treatments enable direct control of surface work function. (a) Atomic ratios as determined by XPS on control and treated $n = 1$ films normalized to I content corroborate the effect of PbI_2 and PEAI film surface treatments. *C atomic ratios are reduced to 25% of their actual magnitude in the plot for improved visual comparison. (b) The photoemission onset in UPS varies for increasing PEAI concentration in treatments of $n = 1$ films. This reflects the upshifting of energy levels and, consequently, a reduction in Wf or IE. (c) X-ray diffraction (XRD) on control and treated films indicates that the film is still pure-phase post-treatments. (d) DFT confirms energy level upshifts as a result of increased coverage of PEAI on both (001) and (100) RDP surfaces.

UPS measurements on control, PEAI-treated (Figures 3b and S1), and PbI_2-treated (Figure S2) $n = 1$ films reveal that only PEAI treatments are able to significantly modify the Wf of RDPs, by up to 1 eV. The magnitude of the band upshift can be controlled by varying the concentration of PEAI up to 6 mg/mL in the treatment solution. The band upshift can be observed in both the photoemission onset as well as the shifts in the valence spectral peaks (of predominantly I and organic character according to Figure 1d). Beyond 6 mg/mL, however, both the photoemission onset and valence spectral peaks blur and are difficult to discern (Figure S1). Previous studies have found RDP films to exhibit phase inhomogeneities, a finding assigned to fast solvent evaporation and nucleation/growth rates,(47,48) and inhomogeneous ligand distribution before annealing(27) in spin-cast RDP films. Our UPS measurements were therefore performed with a large 2.5 mm spot size, and as a result represent average valence spectra across a large area of film.

Previous work has found that increasing I_2 concentration in PEA_2PbI_4 can lead to new crystalline phases.(40) Therefore, we measured XRD on our post-treatment films to ensure that the phase purity of our $n = 1$ film had not been altered (Figure 3c).

We corroborated the effect of ligand concentration at RDP surfaces to upshift its bands and thus reduce Wf and IE by DFT calculations (Figures 3d and S4). We calculated the change in IE by modifying the concentration of PEAI at both (001) and (100) surfaces of an $n = 1$ structure. We found that the IE and Wf indeed decreased with increased PEAI at the surface, which is in agreement with our photoemission studies on PEAI-treated RDP films. Interestingly, the magnitude of the upshift can vary depending on the surface where the ligand is adsorbed. DFT calculations also confirmed that BTAI has essentially the same effect on BTA-based RDPs (Figure S5).

These observations agree with our hypothesis where SCDMs effected by ammonium halide-terminated ligands at the surface are able to misalign RDP energy levels. Beyond a surface saturation point, however, increasing the ligand concentration leads to broadening and blurring of features in the valence spectra. This could be attributed to two effects, each of which could counteract the SCDMs inhomogeneously throughout the film: (1) Increasing ligand concentration beyond the saturation point may lead to unoriented PEAI ligands on the surface. The disordered nature of dipole moments in this scenario would also explain the broadening and blurring of valence spectral features. (2) The limit in SCDM-mediated upshifts could also be attributed to unattached PEAI ligands beyond a saturation point, which would then have limited effects on surface charge redistribution.

PbI_2-treatment on the other hand leads to a negligible effect in the band alignment. The lack of SCDMs could be attributed to the absence of a strong dipole given the low incidence of PEAI surfaces, or to the limited interaction of PbI_2 with undercoordinated surface sites.

The XPS ratios suggest that all corner-shared sites of the control $n = 1$ film are passivated (i.e., there are >2 N atoms for every Pb atom) and that there are no I-vacancies (i.e., there are >4 I atoms for every Pb atom). Therefore, it is most likely that the PEAI treatments passivate interstitial I-sites on the 2D plane (right-most schematic in Figure 2a), as well as passivating edge I-sites. However, RDP films have been found to be inhomogeneous,[27] such that there could be a number of unpassivated I-sites on the 2D plane. Thus, it is possible for the unpassivated structures depicted in Figure 3d to form, despite their higher enthalpies of formation (Table S1), in light of their kinetic (as opposed to thermodynamic) controlled growth.[17,27,47,48] In this scenario, PEAI treatments will first passivate these I-sites before covering interstitial and edge I-sites.

These findings could offer a more likely explanation for the UPS discrepancy in the literature discussed earlier. Different film-deposition techniques and ligand concentrations used in synthesis might alter the surface of RDP films by increasing ligand-rich surfaces relative to PbI_2-rich surfaces, dramatically altering the photoemission onset for films that might otherwise exhibit fairly similar properties. Furthermore, these film treatments have direct implications on perovskite semiconductor device design. Alkyl- and phenyl alkylammonium halide ligands offer interfacial layers to modify the interface between perovskite, transport layers, and contacts in order to improve charge transport and balance, as well as to reduce parasitic resistances.

An implication to note is that RDP–RDP interfaces will exhibit SCDM-mediated misalignments only if the RDP surfaces exhibit different ligand concentrations. However, 2D/3D interfaces will inherently exhibit misalignments due to the contrasting nature of the surfaces incurred in the interface, i.e., the bulk surface is depleted of ligand contrary to the RDP surface. As a result, a 2D/3D interface is more likely to exhibit a type-II interface. This point is verified by contrasting the photoemission onset of bulk and an $n = 20$ sample (Figure S3). The valence band edge of the RDP sample is higher than that of the bulk sample, which can be attributed to the presence of PEAI-passivated surfaces in the former.

Observed Transfer in Type-II Interfaces

We posited whether SCDM-mediated band upshifts could also manifest unintentionally within RDP films without treatments due to varying ligand distribution throughout the film during RDP formation.(27) For example, the alignment between $n = 2$ and $n = 3$ RDPs in a given thin film, assuming homogeneous and equal ligand coverage on both RDP surfaces, should be type-I and therefore lead to exciton and charge transfer solely from $n = 2$ to $n = 3$. However, if some of the $n = 2$ QWs have upshifted bands due to increased ligand coverage, this could potentially result in type-II alignment relative to neighboring $n = 3$ QWs, facilitating hole transfer from $n = 3$ to $n = 2$.

We also noted that a type-II alignment between an upshifted $n = x$ RDP and unshifted $n = x + 1$ would not necessarily mean a type-II alignment between the same upshifted $n = x$ well and an unshifted $n \geq x + 2$, as the energy of the valence band states in the $n \geq x + 2$ wells could still be higher than the upshifted energies of the $n = x$ well (Figure 4). If this were the case, then one could anticipate that direct photoexcitation of the $n = x$ RDP in a transient absorption experiment should result in dynamic photobleaching of $n = x - 1$ wells due to favorable hole transfer; however, hole transfer to $n \leq x - 2$ wells may not be thermodynamically favorable. In the case that type-I alignment persisted between all RDPs in a thin film, no dynamic photobleaching at energies above the photoexcitation pulse would be observed because hole transfer from high-to-low n would be globally disfavored. Conversely, if type-II alignment persisted between all RDPs, then hole transfer would categorically take place from high-to-low n (i.e., regardless of photoexcitation energy) instead.
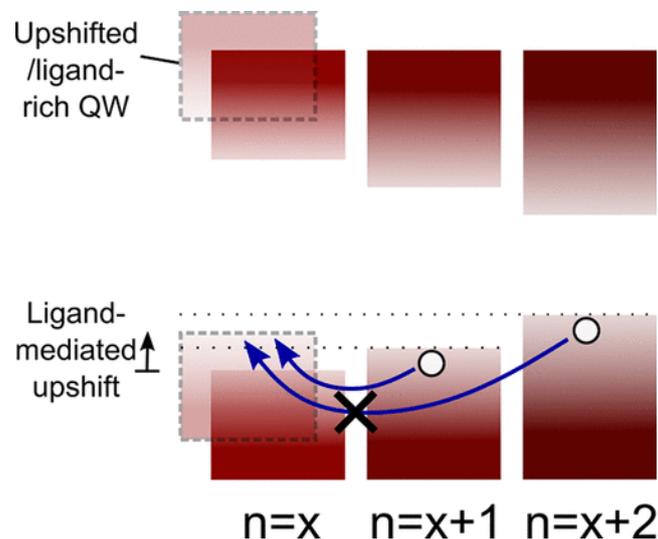
Figure 4. Band upshifts induce type-II interfaces for some but not all RDPs. In this scenario, for instance, the band upshift in $n = x$ induces type-II interfaces with neighboring $n = x + 1$ QWs but maintains interfaces of type-I character with $n = x + 2$ QWs. The latter allows for hole transfer from high-n to low-n.

Ultrafast transient absorption (TA) experiments were performed by selectively photoexciting $n = 2, 3, 4, 5,$ and $6+$ RDPs (Figure 5). Insets in each panel contain a spectral region that is normalized at an arbitrary positive peak in order to more clearly demonstrate peaks that change in relative magnitude over time. For example, in panel e, the bleach peak at 640 nm for $n = 4$ clearly grows relative to the normalized point over time, whereas other peaks for $n = 2$ and $n = 3$ are overlapped at each time point when normalized. This indicates a dynamic process (hole transfer) increasing the bleach signal from $n = 4$.
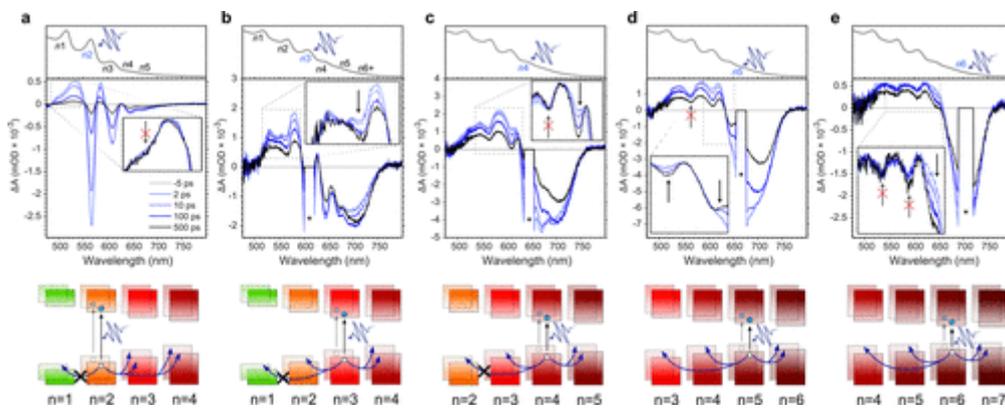

Figure 5. TA on RDPs with varying photoexcitation energies reveals transfer enabled by ligand-mediated shifts. TA spectra of $n = 2$ (a) and $n = 3$ (b–e) samples where photoexcitation energy matches the bandgap of $n = 2$ (a), $n = 3$ (b), $n = 4$ (c), $n = 5$ (d), and $n = 6$ (e). The series reveals that, although exciton transfer should take place primarily toward higher-n phases (which is indeed observed in these experiments), ligand-mediated upshifts can allow a small subset of hole transfer toward lower-n phases (as observed by increasing bleach intensity over time). The asterisk denotes the region of the spectrum hidden by the excitation scatter. Insets contain normalized spectra to more clearly demonstrate which peaks undergo dynamical changes in bleaching signal with time (denoted by black arrows) and which peaks remain relatively unchanged over time (denoted by red-crossed black arrows). The band schematics depict the observed transfer for each case.

In all cases but one, dynamic bleaching is observed for the $n = x - 1$ excitonic resonances over tens of picoseconds due to hole transfer resulting from type-II band alignment, whereas dynamic bleaching of the $n = x - 2$ peaks is often absent, and it never occurred for $n \leq x - 3$ within our range of experiments. Our experiments, however, do not necessarily preclude the latter from taking place. To illustrate our observations, let us focus on photoexcitation of $n = 5$ (Figure 5d). This results in transient bleaching of the $n = 3$ and 4 peaks but does not affect $n = 2$. Similarly, lower-energy photoexcitation at $n = 6+$ (Figure 5e) causes transient bleaching of $n = 4$ and 5 but not $n = 2$ and 3. The single exception is that of the $n = 1$ peak, which is never bleached by any sub-bandgap photoexcitation, strongly suggesting that type-II alignment between $n = 1$ and all other RDPs has a low probability of occurring. In all cases,

it is noted that the population of upshifted RDPs that can act as hole acceptors is small relative to the total population of unshifted wells, assessed from the peak amplitude in absorption spectra.

These results do not agree with total and unconditional type-I nor type-II RDP alignments. These observations are instead consistent with our hypothesis that a minority population of each of the RDPs can have their energy bands upshifted to the extent that they switch from a type-I to type-II alignment relative to RDPs with smaller bandgaps. On the basis of the observed transfer, we conclude that the induced upshifts are between 100 and 200 meV. This is deduced from the fact that photoexcitation at $n = 3$ enables back-transfer toward $n = 2$ (which exhibits a valence band offset $\Delta VB = 0.1$ eV); however, photoexcitation at $n = 2$ does not allow for back-transfer to $n = 1$ ($\Delta VB = 0.2$ eV). The magnitude of the upshift is determined by the contrast of ligand on neighboring RDP surfaces. As a result, the surfaces have a low probability of exhibiting strong contrasts within an RDP film. Therefore, it is expected that upshifts formed unintentionally in RDP films are limited to a few 100 meV.

Discussion

It is here reported that ligand-mediated SCDMs can lead to Wf shifts in RDPs. These SCDMs consist of contributions of similar magnitudes imparted by (1) oriented dipole moments between surface interfaces and (2) surface charge redistribution due to species adsorption.

The material framework presented sheds new light on how both type-I and type-II alignments can arise in RDP thin films, explaining the conflicting results in the literature: funneling[19,25,26] and high PLQY[20,49] in support of type-I, and transfer from high-n to low-n[4,24] and low-n QWs acting as hole traps in support of type-II.[24] This is in addition to studies explicitly finding type-I[19,22] and type-II alignments.[7,19,21] Ligand-mediated band shifts can be systematically controlled to adjust band alignments to design a semiconductor device but can also form inadvertently in RDP films due to inhomogeneous ligand distribution during crystal formation.

The capability of ligand distributions on neighboring surfaces to induce band shifts also helps one to understand the success of RDPs in a wide range of applications. In well-passivated films with a high degree of mixed-dimensionality used for light emission, type-I alignment can dominate the photophysical dynamics due to ligand homogeneity. In some light-emission applications, additives are used to improve passivation,[20,50,51] further mitigating ligand contrasts and band offsets. These ensure high PLQY but also type-I interfaces among RDPs.

In higher-n films with flatter energy landscapes used for solar cells, e.g., $\langle n \rangle = 10$ or 20, the occasional presence of an upshifted low-n RDP leads to type-II alignment that can render it into a trap for holes.[4,21,24,30,31] Even more pertinent to modern perovskite photovoltaic device architectures are mixed 2D/3D heterostructures, which are being increasingly investigated due to improved photovoltages and operational stability.[1,2,16,18] Our results indicate that these systems have a high probability of exhibiting type-II interfaces due to the inherent differences in ligand concentration at the 2D/3D interface. These interfaces can thus be engineered to benefit vertical charge transport, as in the use of an electron-blocking layer, for instance, or could inadvertently lead to hysteresis and traplike states.[4,24,27]

We sought to corroborate the effect of a 2D/3D interface in PV devices (Figure S11). We fabricated photovoltaic devices with and without a thin 2D layer atop bulk perovskite. In the former scenario, holes must be able to pass through the 2D perovskites in order to get to the hole-selective contact (Spiro). This requires a type-II alignment between the 3D and 2D components. In the case that the 2D bands remained unshifted and instead formed a type-I heterojunction with the 3D perovskite, we would expect the hole extraction to be completely suppressed. This was observed in a study by Polander et al.,(52) where a hole-selective layer with a valence band edge 0.2 eV below that of the perovskite active layer resulted in a solar cell efficiency of 0.08% due to an almost complete loss of J_{sc} and fill factor. Instead, J_{sc} is only slightly reduced, and fill factor, Voc, and PCE are each improved with the addition of a thin 2D layer.

Conclusion

In summary, we propose a mechanism of dipole-mediated band misalignments occurring spontaneously in thin films of mixed RDPs that is able to reconcile otherwise incompatible observations of both type-I and type-II alignments throughout the literature. We first report type-I band alignment among RDPs by mitigating common sources of error and misinterpretation, including analyzing single crystals, determining the onset of photoemission with a logarithmic y-axis, and measuring crystals with RDPs aligned parallel to the substrate to avoid surface-dependent photoemission onset variations. On the basis of DFT calculations, we then propose a model that explains the variations that have been measured in energy-level alignments of RDPs in the literature consisting of SCDM-mediated Wf shifts enacted by charge across the ligands. This model is verified experimentally by treating $n = 1$ films by increasing the relative incidence of PEAI and PbI_2 surfaces by solution-processed spin-cast treatments, leading to shifts in the valence band edge of up to 1 eV. Finally, simultaneous type-I and type-II alignments induced by Wf shifts are observed experimentally in untreated RDP films by TA measurements. These measurements validate our hypothesis that these misalignments can occur inadvertently in solution-processed RDP films due to ligand inhomogeneity across the film, and we find that band upshifts of 100–200 meV occur unintentionally in untreated RDP films. Our work explains contrasting behavior of RDPs in LEDs and PV in the literature, where materials can exhibit either type-I or type-II interfaces depending on the ligand concentration at neighboring surfaces.

Methods

Single-Crystal Growth

The $n = 1$, 2, and 3 single crystals were grown following previously reported protocols.(53) A mixture of HI solution (57% wt % in H_2O; 10.0 mL) and 50% aqueous H_3PO_2 (1.7 mL) was heated to 160 °C. PbO powder (2232 mg) was added to the solution and stirred for 5 min. After the powder was fully dissolved, CH_3NH_3Cl powder (450 mg for $n = 3$, 338 mg for $n = 2$, and 0 mg for $n = 1$) was added to the yellow solution and readily redissolved. Separately, butylamine (327 μL for $n = 3$, 694 μL for $n = 2$, and 924 μL for $n = 1$) or phenethylamine (416 μL for $n = 3$, 883 μL for $n = 2$, and 1175 μL for $n = 1$) was slowly mixed with HI (57% wt %

in H_2O; 5.0 mL). The resulting solution was then added to the heated solution. A precipitate was formed and quickly redissolved. The solution was heated for another 2 min to fully dissolve all precipitate. Afterward, the heating and stirring were discontinued, and the solution was allowed to cool to room temperature. In this time, the RDPs crystallized on the surface of the solution. The crystals were extracted, rinsed with hexane, and thoroughly dried in a vacuum chamber.

Film Preparation

The appropriate stoichiometric quantities of PbI_2, MAI, and PEAI were dissolved in 1:1 volume ratio γ-butyrolactone/dimethyl sulfoxide (DMSO) (for films of $\langle n \rangle \geq 10$) or dimethylformamide (DMF) (for $\langle n \rangle < 10$) at 70 °C for 1 h with vigorous stirring. The resulting solution was filtered with a PTFE syringe filter (0.2 μm) before deposition. The next step depended on whether DMF or DMSO was used:

• DMF: The solution was then deposited onto the substrate and spin-coated at 5000 rpm for 20 s. The resulting films were annealed at 70 °C immediately thereafter for 10 min.

• DMSO: The solution was then deposited onto the substrate via a consecutive two-step spin-coating process at 1000 and 5000 rpm for 10 and 60 s, respectively. Halfway into the second spin step, 200 μL of chlorobenzene was deposited onto the substrate. The resulting films were annealed at 70 °C immediately thereafter for 10 min.

Film Treatment

Treatment solutions were prepared by dissolving PEAI or PbI_2 in IPA. The treatment solution was then subsequently dropped onto the substrate and held for 5 s, after which the film was spin-casted at 5000 rpm for 20 s.

Photoelectron Spectroscopy

Both X-ray and ultraviolet photoelectron spectroscopy were measured in an Escalab Xi+ Microprobe system. The XPS measurements were carried with an Al Kα source with a spot size of 900 μm and energy steps of 0.05 eV. The ultraviolet photoelectron spectroscopy measurements were carried out with a He 1α source with a spot size of 2.5 mm and energy steps of 0.02 eV. Film samples were spun on ITO substrates, and a corner of the film was scratched where electrically conductive carbon tape was adhered to avoid charging. All UPS measurements were conducted with a 5 V bias. Single-crystal samples were fixated onto the holder by carbon tape. The ultraviolet photoelectron spectroscopy measurements were carried out first followed by the XPS measurements within the same pump-down so as to avoid sample damage by the latter on the former, more surface-sensitive measurement.

Transient Absorption Spectroscopy

A regeneratively amplified Yb:KGW laser (PHAROS, Light Conversion) was used to generate femtosecond laser pulses at a wavelength of 1030 nm as the fundamental beam with a repetition rate of 5 kHz. The fundamental beam was passed through a beam splitter, where the majority of the beam was used to pump an optical parametric amplifier (ORPHEUS, Light

Conversion) to serve as a narrow-band pump (pulse duration ~200 fs, bandwidth ~10 nm fwhm), which ranged between 400 and 750 nm in order to selectively excite each of the various RDPs. The remaining part of the beam was focused into a translating sapphire crystal in order to generate a white light probe ranging between 450 and 950 nm. The pump and probe pulses were directed into a commercial transient absorption spectrometer (Helios, Ultrafast). The probe pulse was sent to a retroreflector mounted on a delay stage, where multiple reflections off the retroreflector allowed for a delay relative to the pump pulse of up to 8 ns. Measurements were performed with pump powers of 100 μW for each photoexcitation wavelength (570, 610, 645, 666, and 700 nm corresponding to n = 2, 3, 4, 5, and 6+, respectively) with a spot size of 0.30 μm^2 (assuming a Gaussian beam profile).

Computational Details

First-principles calculations based on density functional theory (DFT) were carried out as implemented in the PWSCF Quantum-Espresso package. For geometry optimization, we used the PBE functional;[54] electron–ion interactions were described by ultrasoft pseudopotentials with electrons from I 5s, 5p; N, C 2s, 2p; H 1s; Pb, 6s, 6p, 5d; shells were explicitly included in calculations. Geometry optimizations were done with a $4 \times 4 \times 1$ k-point sampling using experimental cell parameters for all bulk and 001 surfaces structures, and $4 \times 1 \times 1$ for 100 surfaces.

Electronic structure was calculated by single-point hybrid calculations including spin–orbit coupling (SOC) unless otherwise specified. These were conducted using the modified version of the HSE06 functional[55] including 43% Hartree–Fock exchange[56] with norm-conserving pseudo-potentials with electrons from I 5s, 5p; N, C 2s, 2p; H 1s; Pb 5s, 5p, 6s, 6p, 5d; shells were explicitly included in calculations, with $2 \times 2 \times 1$ k-point sampling. This is shortened to HSE throughout the manuscript for conciseness.

Density of states (DOS) of the n = 1–3 perovskites have been aligned with respect to the lowest-energy peak of butyl and benzylic carbon of BTA and PEA, respectively. Work function values for the ligand-saturated and -depleted cases were calculated on five-layered BTA-n = 1 and PEA-n = 1 surface structures and aligned with the valence band position (HSE-SOC) of the corresponding bulk BTA-n = 1 and PEA-n = 1 systems, respectively. In these simulations, the central layer was used to determine the work function.

Supporting Information
The Supporting Information is available free of charge on the ACS Publications website at DOI: 10.1021/jacs.9b04801.

References

1. Jung, E. H.; Jeon, N. J.; Park, E. Y.; Moon, C. S.; Shin, T. J.; Yang, T.-Y.; Noh, J. H.; Seo, J. Efficient, Stable and Scalable Perovskite Solar Cells Using poly(3-Hexylthiophene). Nature 2019, 567, 511– 515, DOI: 10.1038/s41586-019-1036-3

2. Jiang, Q.; Zhao, Y.; Zhang, X.; Yang, X.; Chen, Y.; Chu, Z.; Ye, Q.; Li, X.; Yin, Z.; You, J. Surface Passivation of Perovskite Film for Efficient Solar Cells. Nat. Photonics 2019, 13, 460– 466, DOI: 10.1038/s41566-019-0398-2

3. Tsai, H.; Nie, W.; Blancon, J.-C.; Stoumpos, C. C.; Asadpour, R.; Harutyunyan, B.; Neukirch, A. J.; Verduzco, R.; Crochet, J. J.; Tretiak, S.; Pedesseau, L.; Even, J.; Alam, M. A.; Gupta, G.; Lou, J.; Ajayan, P. M.; Bedzyk, M. J.; Kanatzidis, M. G.; Mohite, A. D. High-Efficiency Two-Dimensional Ruddlesden–Popper Perovskite Solar Cells. Nature 2016, 536, 312– 316, DOI: 10.1038/nature18306

4. Proppe, A. H.; Quintero-Bermudez, R.; Tan, H.; Voznyy, O.; Kelley, S. O.; Sargent, E. H. Synthetic Control over Quantum Well Width Distribution and Carrier Migration in Low-Dimensional Perovskite Photovoltaics. J. Am. Chem. Soc. 2018, 140, 2890– 2896, DOI: 10.1021/jacs.7b12551

5. Lin, K.; Xing, J.; Quan, L. N.; de Arquer, F. P. G.; Gong, X.; Lu, J.; Xie, L.; Zhao, W.; Zhang, D.; Yan, C.; Li, W.; Liu, X.; Lu, Y.; Kirman, J.; Sargent, E. H.; Xiong, Q.; Wei, Z. Perovskite Light-Emitting Diodes with External Quantum Efficiency Exceeding 20 per Cent. Nature 2018, 562, 245– 248, DOI: 10.1038/s41586-018-0575-3

6. Chiba, T.; Hayashi, Y.; Ebe, H.; Hoshi, K.; Sato, J.; Sato, S.; Pu, Y.; Ohisa, S.; Kido, J. Anion-Exchange Red Perovskite Quantum Dots with Ammonium Iodine Salts for Highly Efficient Light-Emitting Devices. Nat. Photonics 2018, 12, 681– 688, DOI: 10.1038/s41566-018-0260-y

7. Li, Z.; Chen, Z.; Yang, Y.; Xue, Q.; Yip, H. L.; Cao, Y. Modulation of Recombination Zone Position for Quasi-Two-Dimensional Blue Perovskite Light-Emitting Diodes with Efficiency Exceeding 5%. Nat. Commun. 2019, 10, 1027, DOI: 10.1038/s41467-019-09011-5

8. Yakunin, S.; Protesescu, L.; Krieg, F.; Bodnarchuk, M. I.; Nedelcu, G.; Humer, M.; De Luca, G.; Fiebig, M.; Heiss, W.; Kovalenko, M. V. Low-Threshold Amplified Spontaneous Emission and Lasing from Colloidal Nanocrystals of Caesium Lead Halide Perovskites. Nat. Commun. 2015, 6, 8056, DOI: 10.1038/ncomms9056

9. Evans, T. J. S.; Schlaus, A.; Fu, Y.; Zhong, X.; Atallah, T. L.; Spencer, M. S.; Brus, L. E.; Jin, S.; Zhu, X. Y. Continuous-Wave Lasing in Cesium Lead Bromide Perovskite Nanowires. Adv. Opt. Mater. 2018, 6, 1700982, DOI: 10.1002/adom.201700982

10. Wehrenfennig, C.; Eperon, G. E.; Johnston, M. B.; Snaith, H. J.; Herz, L. M. High Charge Carrier Mobilities and Lifetimes in Organolead Trihalide Perovskites. Adv. Mater. 2014, 26, 1584– 1589, DOI: 10.1002/adma.201305172

11. Brandt, R. E.; Poindexter, J. R.; Gorai, P.; Kurchin, R. C.; Hoye, R. L. Z.; Nienhaus, L.; Wilson, M. W. B.; Polizzotti, J. A.; Sereika, R.; Žaltauskas, R.; Lee, L. C.; Macmanus-Driscoll, J. L.; Bawendi, M.; Stevanović, V.; Buonassisi, T. Searching For "defect-Tolerant"

Photovoltaic Materials: Combined Theoretical and Experimental Screening. Chem. Mater. 2017, 29, 4667– 4674, DOI: 10.1021/acs.chemmater.6b05496

12. Shi, D.; Adinolfi, V.; Comin, R.; Yuan, M.; Alarousu, E.; Buin, A.; Chen, Y.; Hoogland, S.; Rothenberger, A.; Katsiev, K.; Losovyj, Y.; Zhang, X.; Dowben, P. A.; Mohammed, O. F.; Sargent, E. H.; Bakr, O. M. Low Trap-State Density and Long Carrier Diffusion in Organolead Trihalide Perovskite Single Crystals. Science 2015, 347, 519– 522, DOI: 10.1126/science.aaa2725

13. Kovalenko, M. V.; Protesescu, L.; Bodnarchuk, M. I. Properties and Potential Optoelectronic Applications of Lead Halide Perovskite Nanocrystals. Science 2017, 358, 745– 750, DOI: 10.1126/science.aam7093

14. Mitzi, D. B. Progress in Inorganic Chemistry; Wiley: 1999; Vol. 48.

15. Mitzi, D. B.; Feild, C. a.; Harrison, W. T. a.; Guloy, a. M. Conducting Tin Halides with a Layered Organic-Based Perovskite Structure. Nature 1994, 369, 467– 469, DOI: 10.1038/369467a0

16. Grancini, G.; Roldán-Carmona, C.; Zimmermann, I.; Mosconi, E.; Lee, X.; Martineau, D.; Narbey, S.; Oswald, F.; De Angelis, F.; Graetzel, M.; Nazeeruddin, M. K. One-Year Stable Perovskite Solar Cells by 2D/3D Interface Engineering. Nat. Commun. 2017, 8, 15684, DOI: 10.1038/ncomms15684

17. Quan, L. N.; Yuan, M.; Comin, R.; Voznyy, O.; Beauregard, E. M.; Hoogland, S.; Buin, A.; Kirmani, A. R.; Zhao, K.; Amassian, A.; Kim, D. H.; Sargent, E. H. Ligand-Stabilized Reduced-Dimensionality Perovskites. J. Am. Chem. Soc. 2016, 138, 2649– 2655, DOI: 10.1021/jacs.5b11740

18. Cho, K. T.; Zhang, Y.; Orlandi, S.; Cavazzini, M.; Zimmermann, I.; Lesch, A.; Tabet, N.; Pozzi, G.; Grancini, G.; Nazeeruddin, M. K. Water-Repellent Low-Dimensional Fluorous Perovskite as Interfacial Coating for 20% Efficient Solar Cells. Nano Lett. 2018, 18, 5467– 5474, DOI: 10.1021/acs.nanolett.8b01863

19. Yuan, M.; Quan, L. N.; Comin, R.; Walters, G.; Sabatini, R.; Voznyy, O.; Hoogland, S.; Zhao, Y.; Beauregard, E. M.; Kanjanaboos, P.; Lu, Z.; Kim, D. H.; Sargent, E. H. Perovskite Energy Funnels for Efficient Light-Emitting Diodes. Nat. Nanotechnol. 2016, 11, 872– 877, DOI: 10.1038/nnano.2016.110

20. Ban, M.; Zou, Y.; Rivett, J. P. H.; Yang, Y.; Thomas, T. H.; Tan, Y.; Song, T.; Gao, X.; Credgington, D.; Deschler, F.; Sirringhaus, H.; Sun, B. Solution-Processed Perovskite Light Emitting Diodes with Efficiency Exceeding 15% through Additive-Controlled Nanostructure Tailoring. Nat. Commun. 2018, 9, 3892, DOI: 10.1038/s41467-018-06425-5

21. Cao, D. H.; Stoumpos, C. C.; Farha, O. K.; Hupp, J. T.; Kanatzidis, M. G. 2D Homologous Perovskites as Light-Absorbing Materials for Solar Cell Applications. J. Am. Chem. Soc. 2015, 137, 7843– 7850, DOI: 10.1021/jacs.5b03796

22. Silver, S.; Yin, J.; Li, H.; Brédas, J. L.; Kahn, A. Characterization of the Valence and Conduction Band Levels of N = 1 2D Perovskites: A Combined Experimental and Theoretical Investigation. Adv. Energy Mater. 2018, 8, 1703468, DOI: 10.1002/aenm.201703468

23. Harrison, P. Quantum Wells, Wires and Dots - Theoretical and Computational Physics; Wiley: 2005.

24. Liu, J.; Leng, J.; Wu, K.; Zhang, J.; Jin, S. Observation of Internal Photoinduced Electron and Hole Separation in Hybrid 2-Dimentional Perovskite Films. J. Am. Chem. Soc. 2017, 139, 1432– 1435, DOI: 10.1021/jacs.6b12581

25. Wei, M.; de Arquer, F. P. G.; Walters, G.; Yang, Z.; Quan, L. N.; Kim, Y.; Sabatini, R.; Quintero-Bermudez, R.; Gao, L.; Fan, J. Z.; Fan, F.; Gold-Parker, A.; Toney, M. F.; Sargent, E. H. Ultrafast Narrowband Exciton Routing within Layered Perovskite Nanoplatelets Enables Low-Loss Luminescent Solar Concentrators. Nat. Energy 2019, 4, 197– 205, DOI: 10.1038/s41560-018-0313-y

26. Wang, N.; Cheng, L.; Ge, R.; Zhang, S.; Miao, Y.; Zou, W.; Yi, C.; Sun, Y.; Cao, Y.; Yang, R.; Wei, Y.; Guo, Q.; Ke, Y.; Yu, M.; Jin, Y.; Liu, Y.; Ding, Q.; Di, D.; Yang, L.; Xing, G.; Tian, H.; Jin, C.; Gao, F.; Friend, R. H.; Wang, J.; Huang, W. Perovskite Light-Emitting Diodes Based on Solution-Processed Self-Organized Multiple Quantum Wells. Nat. Photonics 2016, 10, 699– 704, DOI: 10.1038/nphoton.2016.185

27. Quintero-Bermudez, R.; Gold-Parker, A.; Proppe, A. H.; Munir, R.; Yang, Z.; Kelley, S. O.; Amassian, A.; Toney, M. F.; Sargent, E. H. Compositional and Orientational Control in Metal Halide Perovskites of Reduced Dimensionality. Nat. Mater. 2018, 17, 900– 907, DOI: 10.1038/s41563-018-0154-x

28. Zhao, L.; Lin, Y. L.; Kim, H.; Giebink, N. C.; Rand, B. P. Donor/acceptor Charge-Transfer States at Two-Dimensional Metal Halide Perovskite and Organic Semiconductor Interfaces. ACS Energy Lett. 2018, 3, 2708– 2712, DOI: 10.1021/acsenergylett.8b01722

29. Xiao, Z.; Zhao, L.; Tran, N. L.; Lin, Y. L.; Silver, S. H.; Kerner, R. A.; Yao, N.; Kahn, A.; Scholes, G. D.; Rand, B. P. Mixed-Halide Perovskites with Stabilized Bandgaps. Nano Lett. 2017, 17, 6863– 6869, DOI: 10.1021/acs.nanolett.7b03179

30. Cho, K. T.; Grancini, G.; Lee, Y.; Oveisi, E.; Ryu, J.; Almora, O.; Tschumi, M.; Schouwink, P. A.; Seo, G.; Heo, S.; Park, J.; Jang, J.; Paek, S.; Garcia-Belmonte, G.; Nazeeruddin, M. K. Selective Growth of Layered Perovskites for Stable and Efficient Photovoltaics. Energy Environ. Sci. 2018, 11, 952– 959, DOI: 10.1039/C7EE03513F

31. Bai, Y.; Xiao, S.; Hu, C.; Zhang, T.; Meng, X.; Lin, H.; Yang, Y.; Yang, S. Dimensional Engineering of a Graded 3D–2D Halide Perovskite Interface Enables Ultrahigh VocEnhanced Stability in the P-I-N Photovoltaics. Adv. Energy Mater. 2017, 7, 1701038, DOI: 10.1002/aenm.201701038

32. Lai, H.; Kan, B.; Liu, T.; Zheng, N.; Xie, Z.; Zhou, T.; Wan, X.; Zhang, X.; Liu, Y.; Chen, Y. Two-Dimensional Ruddlesden–Popper Perovskite with Nanorod-like Morphology for Solar Cells with Efficiency Exceeding 15%. J. Am. Chem. Soc. 2018, 140, 11639– 11646, DOI: 10.1021/jacs.8b04604

33. Lindau, I.; Spicer, W. E. The Probing Depth in Photoemission and Auger-Electron Spectroscopy. J. Electron Spectrosc. Relat. Phenom. 1974, 3, 409– 413, DOI: 10.1016/0368-2048(74)80024-1

34. Endres, J.; Egger, D. A.; Kulbak, M.; Kerner, R. A.; Zhao, L.; Silver, S. H.; Hodes, G.; Rand, B. P.; Cahen, D.; Kronik, L.; Kahn, A. Valence and Conduction Band Densities of States of Metal Halide Perovskites: A Combined Experimental-Theoretical Study. J. Phys. Chem. Lett. 2016, 7, 2722– 2729, DOI: 10.1021/acs.jpclett.6b00946

35. Kawai, H.; Giorgi, G.; Marini, A.; Yamashita, K. The Mechanism of Slow Hot-Hole Cooling in Lead-Iodide Perovskite: First-Principles Calculation on Carrier Lifetime from Electron-Phonon Interaction. Nano Lett. 2015, 15, 3103– 3108, DOI: 10.1021/acs.nanolett.5b00109

36. Smoluchowski, R. Anisotropy of the Electronic Work Function of Metals. Phys. Rev. 1941, 60, 661– 674, DOI: 10.1103/PhysRev.60.661

37. Skriver, H. L.; Rosengaard, N. M. Surface Energy and Work Function of Elemental Metals. Phys. Rev. B: Condens. Matter Mater. Phys. 1992, 46, 7157– 7168, DOI: 10.1103/PhysRevB.46.7157

38. Wu, X.; Trinh, M. T.; Zhu, X. Y. Excitonic Many-Body Interactions in Two-Dimensional Lead Iodide Perovskite Quantum Wells. J. Phys. Chem. C 2015, 119, 14714– 14721, DOI: 10.1021/acs.jpcc.5b00148

39. Blancon, J.; Stier, A. V.; Tsai, H.; Nie, W.; Stoumpos, C. C.; Traoré, B.; Pedesseau, L.; Kepenekian, M.; Katsutani, F.; Noe, G. T.; Kono, J.; Tretiak, S.; Crooker, S. A.; Katan, C.; Kanatzidis, M. G.; Crochet, J. J.; Even, J.; Mohite, A. D. Scaling Law for Excitons in 2D Perovskite Quantum Wells. Nat. Commun. 2018, 9, 2254, DOI: 10.1038/s41467-018-04659-x

40. Smith, M. D.; Pedesseau, L.; Kepenekian, M.; Smith, I. C.; Katan, C.; Even, J.; Karunadasa, H. I. Decreasing the Electronic Confinement in Layered Perovskites through Intercalation. Chem. Sci. 2017, 8, 1960– 1968, DOI: 10.1039/C6SC02848A

41. Vázquez, H.; Gao, W.; Flores, F.; Kahn, A. Energy Level Alignment at Organic Heterojunctions : Role of the Charge Neutrality Level. Phys. Rev. B: Condens. Matter Mater. Phys. 2005, 71, 041306, DOI: 10.1103/PhysRevB.71.041306

42. Dandrea, R. G.; Duke, C. B.; Zunger, A.; Zunger, A. Interfacial Atomic Structure and Band Offsets at Semiconductor Heterojunctions. J. Vac. Sci. Technol., B: Microelectron. Process. Phenom. 1992, 10, 1744, DOI: 10.1116/1.586234

43. Campbell, I. H.; Kress, J. D.; Martin, R. L.; Smith, D. L.; Barashkov, N. N.; Ferraris, J. P. Controlling Charge Injection in Organic Electronic Devices Using Self-Assembled Monolayers. Appl. Phys. Lett. 1997, 71, 3528, DOI: 10.1063/1.120381

44. Campbell, I. H.; Rubin, S.; Zawodzinski, T. A.; Kress, J. D.; Martin, R. L.; Smith, D. L.; Barashkov, N. N.; Ferraris, J. P. Controlling Schottky Energy Barriers in Organic Electronic Devices Using Self-Assembled Monolayers. Phys. Rev. B: Condens. Matter Mater. Phys. 1996, 54, R14321, DOI: 10.1103/PhysRevB.54.R14321

45. Peisert, H.; Knupfer, M.; Fink, J. Energy Level Alignment at Organic/Metal Interfaces : Dipole and Ionization Potential. Appl. Phys. Lett. 2002, 81, 2400, DOI: 10.1063/1.1509472

46. Ronca, E.; Pastore, M.; Belpassi, L.; Tarantelli, F.; De Angelis, F. Influence of the Dye Molecular Structure on the TiO2 Conduction Band in Dye-Sensitized Solar Cells: Disentangling Charge Transfer and Electrostatic Effects. Energy Environ. Sci. 2013, 6, 183– 193, DOI: 10.1039/C2EE23170K

47. Chen, A. Z.; Shiu, M.; Ma, J. H.; Alpert, M. R.; Zhang, D.; Foley, B. J.; Smilgies, D. M.; Lee, S. H.; Choi, J. J. Origin of Vertical Orientation in Two-Dimensional Metal Halide Perovskites and Its Effect on Photovoltaic Performance. Nat. Commun. 2018, 9, 1336, DOI: 10.1038/s41467-018-03757-0

48. Chen, A. Z.; Shiu, M.; Deng, X.; Mahmoud, M.; Zhang, D.; Foley, B. J.; Lee, S.; Giri, G.; Choi, J. J. Understanding the Formation of Vertical Orientation in Two- Dimensional Metal Halide Perovskite Thin Films. Chem. Mater. 2019, 31, 1336– 1343, DOI: 10.1021/acs.chemmater.8b04531

49. La-Placa, M.-G.; Longo, G.; Babaei, A.; Martınez-Sarti, L.; Sessolo, M.; Bolink, H. J. Photoluminescence Quantum Yield Exceeding 80% in Low Dimensional Perovskite Thin-Films via Passivation Control. Chem. Commun. 2017, 53, 8707– 8710, DOI: 10.1039/C7CC04149G

50. deQuilettes, D. W.; Koch, S.; Burke, S.; Paranji, R. K.; Shropshire, A. J.; Ziffer, M. E.; Ginger, D. S. Photoluminescence Lifetimes Exceeding 8 μ S and Quantum Yields Exceeding 30% in Hybrid Perovskite Thin Films by Ligand Passivation. ACS Energy Lett. 2016, 1, 438– 444, DOI: 10.1021/acsenergylett.6b00236

51. Yang, X.; Zhang, X.; Deng, J.; Chu, Z.; Jiang, Q.; Meng, J.; Wang, P.; Zhang, L.; Yin, Z.; You, J. Efficient Green Light-Emitting Diodes Based on Quasi-Two-Dimensional Composition and Phase Engineered Perovskite with Surface Passivation. Nat. Commun. 2018, 9, 570, DOI: 10.1038/s41467-018-02978-7

52. Polander, L. E.; Pahner, P.; Schwarze, M.; Saalfrank, M.; Koerner, C.; Leo, K. Hole-transport material variation in fully vacuum deposited perovskite solar cells. APL Mater. 2014, 2, 081503, DOI: 10.1063/1.4889843

53. Stoumpos, C. C.; Cao, D. H.; Clark, D. J.; Young, J.; Rondinelli, J. M.; Jang, J. I.; Hupp, J. T.; Kanatzidis, M. G. Ruddlesden-Popper Hybrid Lead Iodide Perovskite 2D Homologous Semiconductors. Chem. Mater. 2016, 28, 2852– 2867, DOI: 10.1021/acs.chemmater.6b00847

54. Perdew, J. P.; Burke, K.; Ernzerhof, M. Generalized Gradient Approximation Made Simple. Phys. Rev. Lett. 1996, 77, 3865– 3868, DOI: 10.1103/PhysRevLett.77.3865

55. Heyd, J.; Scuseria, G. E.; Ernzerhof, M. Hybrid Functionals Based on a Screened Coulomb Potential. J. Chem. Phys. 2003, 118, 8207– 8215, DOI: 10.1063/1.1564060

56. Du, M. H. Density Functional Calculations of Native Defects in CH3NH3PbI3: Effects of Spin - Orbit Coupling and Self-Interaction Error. J. Phys. Chem. Lett. 2015, 6, 1461– 1466, DOI: 10.1021/acs.jpclett.5b00199